Sensors & Actuators: A. Physical 363 (2023) 114690

Contents lists available at ScienceDirect

Sensors and Actuators: A. Physical

journal homepage: www.journals.elsevier.com/sensors-and-actuators-a-physical

Performance analysis of on-chip coupled piezo/photodiodes, a numerical study

Nasim Rezaei, Zeinab Eftekhari, Jian-Yao Zheng, Rebecca Saive *

University of Twente, Enschede 7522NB, the Netherlands

ARTICLE INFO

Keywords:
Piezoelectric
Solar cell
Mechanical efficiency
FEM modelling
Light actuation

ABSTRACT

We are presenting a numerical approach to calculate the mechanical efficiency of piezo-photomotion devices, which consist of piezoelectric actuators, integrated with silicon solar cells. Such devices provide conversion of optical energy to mechanical energy and pave the way for remote-controlled micro and nanorobots. We demonstrate that the mechanical efficiency is almost independent of the input voltage and can reach 0.06% under a simple point force load, when the backside etching of the silicon substrate, i.e. the diaphragm is 8 mm in diameter and 30 μm in thickness. This study offers guidelines for future design improvements.

1. Introduction

Untethered mini robots offer many applications in medicine and industry, as they facilitate remote operations in the human body as well as in hostile environments. Such robots can be either remotely powered or have onboard storage. Unlike onboard energy storage, which could limit downsizing of such robots due to typically large battery sizes [1], remote powering provides an opportunity to realize micro and nanorobots. Various actuators have been studied by different research groups for mini robots, including but not limited to shape-memory alloys [2,3], electrostatic [4,5], electromagnetic [6–8], conjugated polymer [9] and piezoelectric actuators [10–13].

In our research group, we are interested in thin-film piezoelectric actuators as they generate substantial force and high actuation with modest amounts of voltage input [14]. Combining this feature with the photovoltaic (PV) effect results in light-driven piezoelectric actuators, which use light as the primary source of energy to achieve motion. In a previous work, we demonstrated an on-chip piezo/photodiode based on silicon technology, which could work both with direct voltage excitation and light illumination [13]. Here, we focus on defining a performance indicative to compare different device architectures, study the effect of the piezoelectric layer dimensions as well as the back-side etching dimensions on mechanical efficiency and finally propose guidelines for future devices.

In such a transducer device, the energy conversion takes place in two steps. First, the optical energy is converted to electrical energy in the PV component, and then, the photogenerated electrical energy is transformed into mechanical displacement. In this process, several loss mechanisms exist, including optical and electrical losses in the solar cell and material losses in the actuator. Energy conversion efficiency is defined as the ratio between the input optical energy and the output mechanical energy, and can be broken down into two multiplying components, i) optical-electrical energy conversion efficiency (η_1), and ii) electrical-mechanical energy conversion efficiency (η_2). In this work, we focus on the second component.

In the following, we firstly introduce the experimental and theoretical techniques used in this project. The model parameters are validated by comparing the simulated displacement with experimentally measured values using atomic force microscopy. We then introduce the mechanical efficiency and its comprising energy components. This is followed by an analysis of the reference piezo-photomotion device and, finally, an investigation of the effect of variations in several geometrical parameters on the mechanical efficiency, free displacement and blocking force.

2. Methods

In this section, our first generation piezo-photomotion devices are briefly described. Then, the details of simulation settings are provided, followed by an explanation to the mechanical efficiency calculations.

2.1. Experiments

The piezo-photomotion device used in the experiments here is based

* Corresponding author.
E-mail address: r.saive@utwente.nl (R. Saive).

https://doi.org/10.1016/j.sna.2023.114690
Received 25 January 2023; Received in revised form 24 April 2023; Accepted 23 September 2023
Available online 26 September 2023

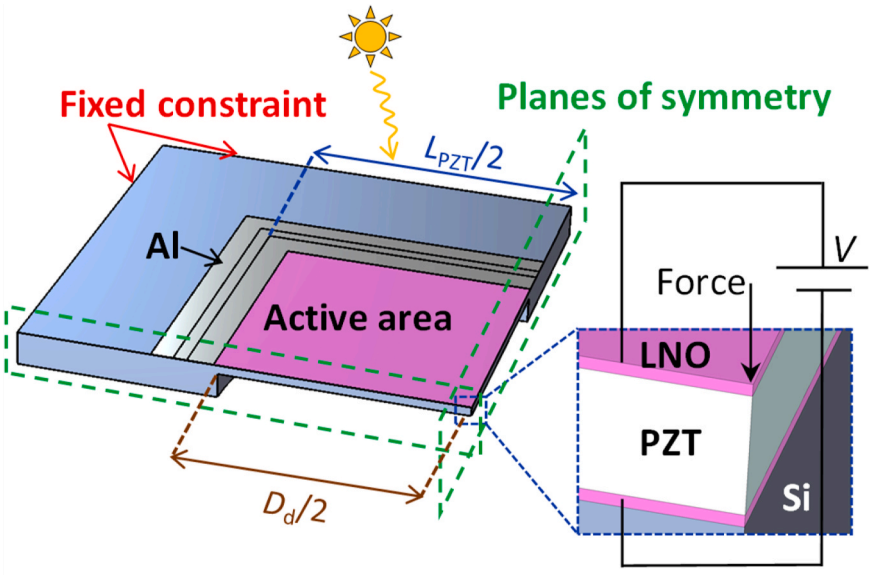

Fig. 1. Visual rendering of the simulated device in COMSOL Multiphysics, Including the boundary conditions.

Table 1
Fabricated and simulated device dimensions.

layer	Silicon	LNO	PZT	Al	SiO_2
Thickness [μm]	380	0.1	1	1.7	1.2
Length/width [mm]	10	6.2	6.2	0.7	0.15

on a previously reported process [13]. It is comprised of a piezoelectric material (PZT) sandwiched between two lanthanum nickelate (LNO) layers and integrated with silicon photodiodes. A schematic of the device structure is shown in Fig. 1. A thin SiO_2 layer at the edges of the piezoelectric stack is used to prevent shunting between the top and bottom LNO layers. Additionally, the underside of the 380-μm thick silicon substrate is circularly etched to reduce the clamping effect on PZT and allow for more displacement. An electric field can be applied to the PZT layer either by light illumination of the photodiode or by direct application of voltage at the terminals. It is instructive to note that regardless of the PZT area, there is always a fixed 1.5 mm distance between the device edge and the top Al electrode. This is to ensure a safe gap for cutting the samples in experiments. This criterion is respected throughout the simulation study.

2.2. Simulations

We used COMSOL Multiphysics for finite element method (FEM) simulations of our devices. Solid mechanics and Electrostatics modules are coupled to facilitate the piezoelectricity calculations. Since the device is symmetrical at least in 2 directions, only one quarter of the structure is modelled in COMSOL in order to reduce the computational costs of the simulations. The symmetry boundary condition is set such that no displacement occurs in the direction normal to the plane of symmetry (see Fig. 1). Analogous to our atomic force microscopy (AFM) measurements, the sample sides are fixed. The impact of gravitational force on the displacement is taken into account. According to our experiments at low frequencies (<10 Hz), in this opto-electro-mechanical system, the electro-mechanical performance is decoupled from the opto-electrical behavior [15]. In other words, the piezoelectric stack is not sensitive to illumination (no mechanical energy is generated due to illumination) and only reacts to the photo-generated voltage at the p-n junction. This feature was exploited in our model to simplify the computations by only taking voltage excitation at the LNO terminals into account. The voltage signal is introduced to the terminals as shown in the inset of Fig. 1.

Table 2
Properties of the PZT film [16,17]. ε_r and ν stand for relative permittivity under constant mechanical stress and Poisson's ratio, respectively. Compliance matrix elements and coupling matrix elements have the units of $\frac{1}{TPa}$ and $\frac{pm}{V}$, respectively.

ε_r	ν	S_{11}	S_{12}	S_{13}	S_{33}	d_{15}	d_{31}	d_{33}
600	0.32	13.8	-4.07	-5.8	20.7	494	-93.5	223

The geometrical dimensions of different layers according to the fabricated device are shown in Table 1. The under-etched section of the Si substrate (the diaphragm) is centered under the LNO/PZT/LNO stack (henceforth known as the piezo stack) and has a diameter (D_d) of 5.5 mm and a thickness (T_d) of 100 μm. The material properties of the thin-film PZT layer were derived from literature and are presented in Table 2. It should be noted that the strain-charge form convention of COMSOL is used in these simulations. The model calibration consisted of adjustments to these geometrical and material parameters such that the measured and simulated displacement reached a close agreement.

The simulated displacement of the fabricated device is compared to the measurements in Fig. 2. The excitation voltage was set to 200 mV, equal to the photo-generated voltage of the device, measured by Kelvin probe force microscopy (KPFM) [15]. It should be noted that as seen in Fig. 1, a narrow part of the piezo stack (0.3 mm around the edges) is covered by the aluminum top electrode and experiences more clamping than the rest of the piezo stack. The uncovered area, which is studied in the AFM measurements is called "the active area". A close resemblance between the measurements and the simulated data confirms the accuracy of the simulations. The displacement at the center of the membrane is one of the figures of merit in this project, and is influenced by two main forces, namely the gravitational load and the piezoelectric force.

2.3. Mechanical efficiency

As briefly explained in the introduction, the energy conversion efficiency of this opto- electro-mechanical system consists of two multiplying components, namely, the optical-electrical energy conversion efficiency (η_1) and the electrical-mechanical energy conversion efficiency (η_2). Although in this work, we do not focus on η_1, it is worth

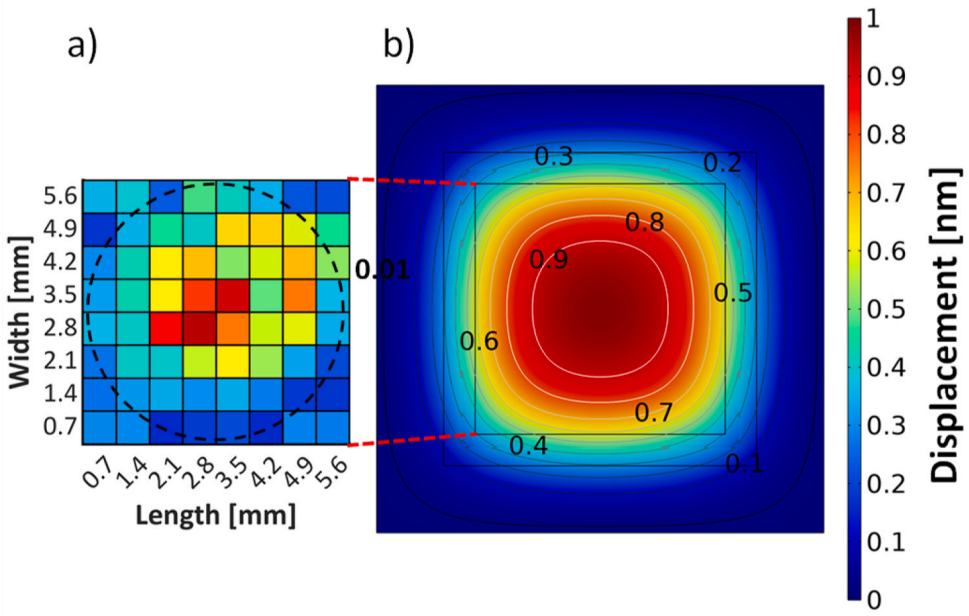

Fig. 2. a) Measured displacement (in nm) in the active area under illumination. The dashed circle marks the diaphragm region. b) simulated displacement under 200 mV voltage excitation. The inner solid square marks the active area equivalent to part a.

providing some insight into this efficiency component as well. The standard efficiency of solar cells is defined via illumination of the solar cells with AM 1.5 G solar spectrum with power density of 1000 W/m^2 [18]. It is calculated by integrating the generated electrical power over the entire AM 1.5 G wavelength spectrum (300–1200 nm). Since we use monochromatic light to excite the solar cell, the concept of spectral efficiency, which represents the efficiency at each wavelength must be used [19–23].

The second efficiency component (η_2) is called the mechanical efficiency here. The performance of a piezoelectric transducer, regardless of whether it is designed as a motor (actuator) or as an energy harvester, which produces electrical energy from input mechanical energy, can be quantified by mechanical efficiency. This metric is defined as the ratio of the output mechanical (electrical) energy to the input electrical (mechanical) energy. While the electrical energy can be determined easily, the mechanical energy in both scenarios is not as easily measured. This has resulted in a discrepancy in the reported energy conversion efficiencies in literature [24–28]. Yang et al. derived an efficiency expression for an energy harvesting system, based on energy flow analysis and validated the model with a piezoceramic energy harvesting cantilever with an efficiency ranging from 6% to 12%, depending on the operation frequency [25]. Shafer et al. showed that the maximum efficiency of a piezoelectric energy harvester depends on mechanical damping and the coupling coefficient and predicted a maximum resonance efficiency of 44% for a cantilever system [26]. Kim et al. analyzed the performance of cantilever piezoelectric vibrating energy harvesting systems and proved that the conditions for maximum power output defer from the conditions for maximum efficiency and both depend on the electrical load as well as piezoelectric properties [27]. Xie et al. developed a one-dimensional model for the efficiency of a piezoelectric energy harvesting cylinder and predicted efficiency values as high as 80%, depending on electrical load conditions [28]. In this respect, for the case of piezoelectric actuators under our study, the analytical calculation of this rather important metric is similarly challenging. Two parameters that comprise the output mechanical power (work done by the actuator) are free displacement and blocking force. In our case, free displacement (Z_f) refers to the displacement (deflection) of the actuator at the center, when no external load apart from gravity is applied, and therefore, no mechanical work is performed. The blocking force (F_b) equals the amount of force exerted by the actuator at the same point, when the deflection is completely suppressed by an external load [29]. There is a linear relationship between the displacement and the exerted force, which is also observed in our simulations [30,31]. Mechanical energy is defined as [31], [32]:

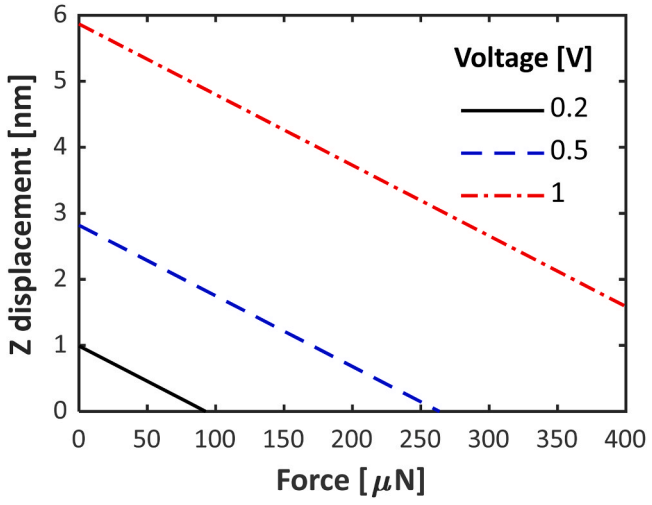

Fig. 3. Midpoint displacement as a function of external load and input voltage. The solid black line represents the fabricated device.

$$W_m = \frac{1}{2} Z_f F_b \tag{1}$$

The mechanical work is zero when either variable is zero and in quasi-static conditions, both free displacement and blocking force have a linear relationship with the input voltage [30]. In simulations, the blocking force is calculated by varying a downward point load applied to the center of the membrane (see Fig. 1) until the central displacement reaches zero. We are aware of the fact that this simplification leads to a considerable underestimation of the total mechanical energy produced by the device and hence, the mechanical efficiency. In other words, the mechanical energy as calculated in this model, is what a point load can probe and not the intrinsic limit of our devices. However, this figure of merit can be easily simulated and also experimentally measured and

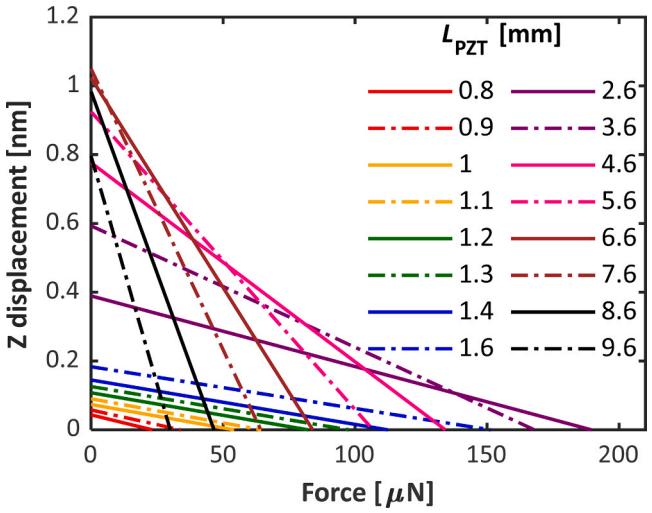

Fig. 4. Midpoint displacement as a function of force and PZT length.

serves well for comparison purposes. In a more complete scenario, the total output energy can be calculated by a point-by-point integration of W_m (Eq. (1)) over the entire active area.

The input electrical energy can be calculated as follows:

$$W_E = \frac{1}{2}QV, \tag{2}$$

where Q is the accumulated charge at the LNO terminal and V is the excitation voltage. The mechanical efficiency, therefore, will be equal to:

$$\eta_M = \frac{W_M}{W_E} \tag{3}$$

3. Results and discussion

3.1. Reference device performance

Fig. 3 presents the midpoint displacement of the reference device under various force and input voltages. A linear trend between each displacement-force line and input voltage is observable [33]. In

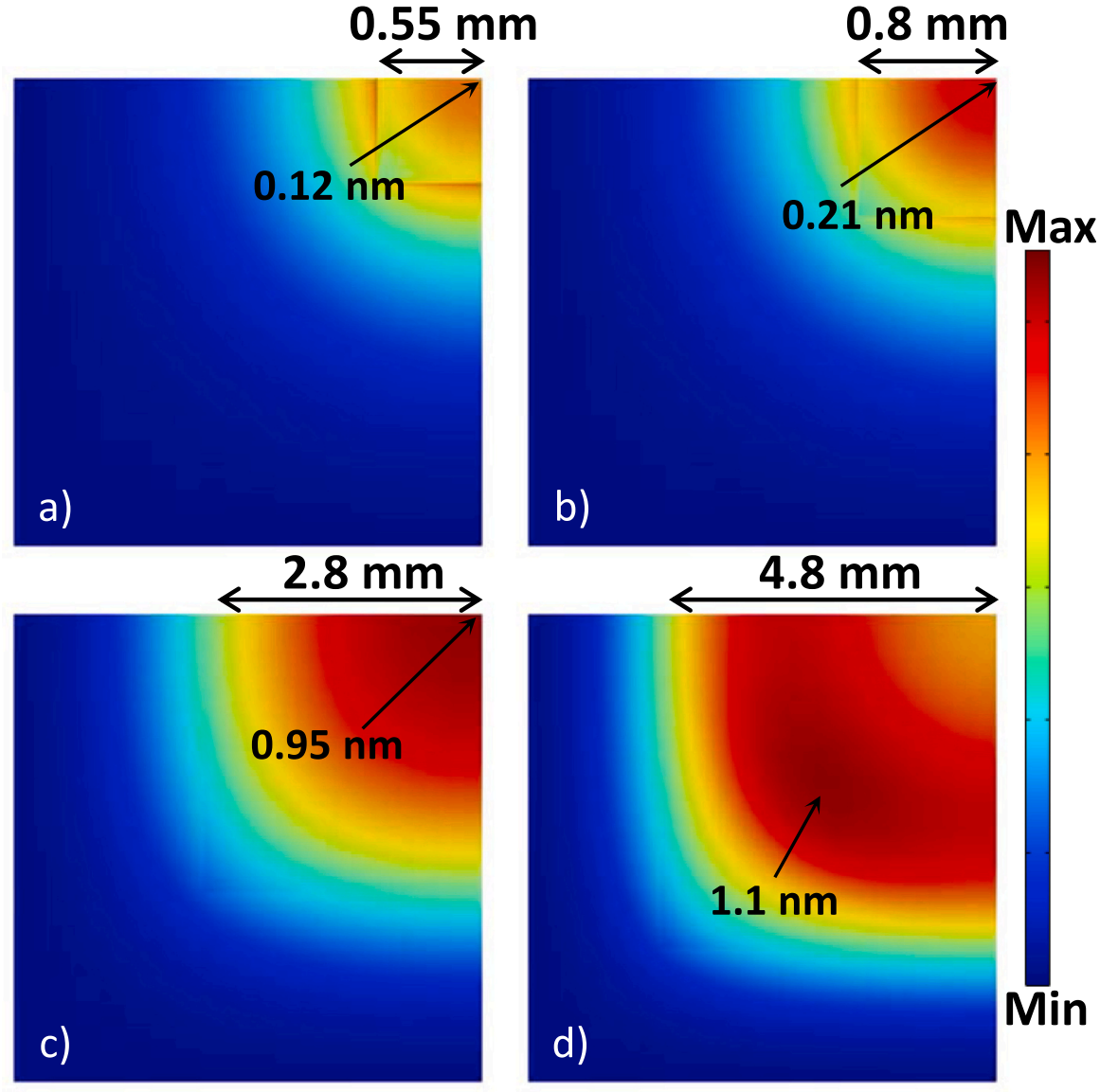

Fig. 5. Displacement mapping for a) L_{PZT} = 1.1 mm, b) L_{PZT} = 1.6 mm, c) L_{PZT} = 5.6 mm and d) L_{PZT} = 9.6 mm. The pictures are not to scale. Small arrows mark the maximum displacement points.

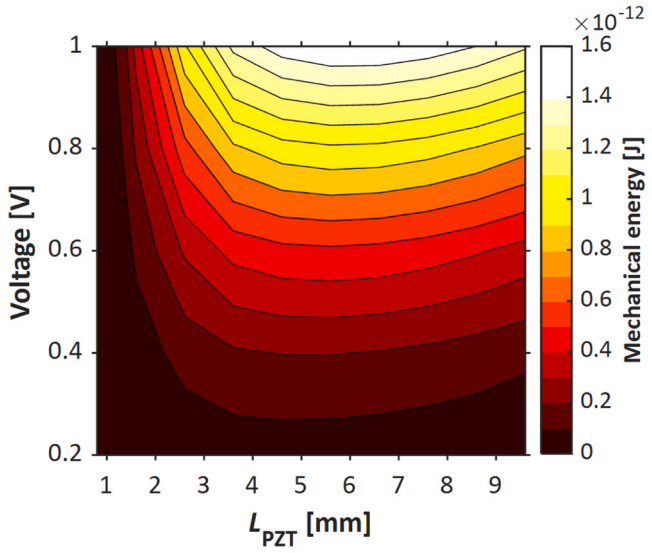

Fig. 6. Simulated mechanical energy as a function of the piezo stack length and input voltage.

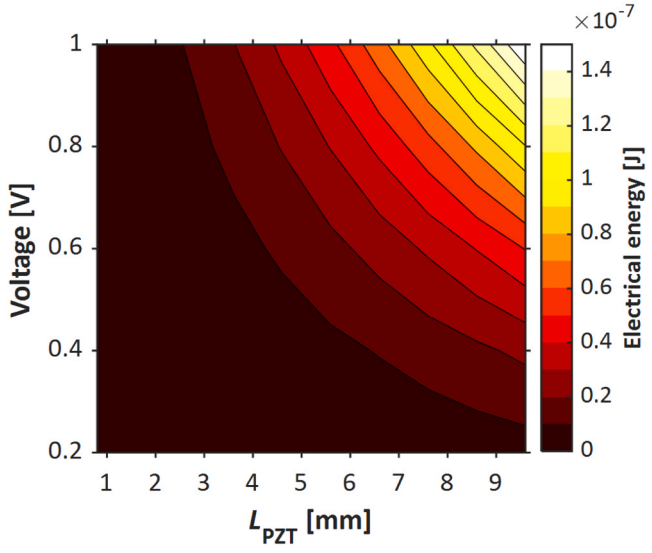

Fig. 7. Simulated electrical energy as a function of the piezo stack length and input voltage.

principle, the input voltage depends on the electrical efficiency of the solar cell and can reach values larger than 1 V [34–36]. The intersection of each line with the y and x axes represents Z_f and F_b, respectively. Using Eqs. (1)–(3), the mechanical efficiency of the reference device under 0.2 V input voltage is calculated and equals to 0.0017%.

3.2. Device area investigation

Since the initial device geometry was chosen without knowing optimal conditions, a sensitivity analysis was performed in order to establish a design guideline for future device generations. In a first step, the impact of the piezo stack length (L_{PZT}) on the displacement-force trends was studied. It should be noted that in these simulations, the diaphragm diameter varies relative to L_{PZT} to maintain a qualitatively constant clamping effect on the piezo stack. As is observed in Fig. 4, when L_{PZT} increases from 0.6 mm to 9.6 mm, there is first an increasing and then a decreasing trend in free displacement. The reason can be related to the interplay between the gravitational force and the exerted

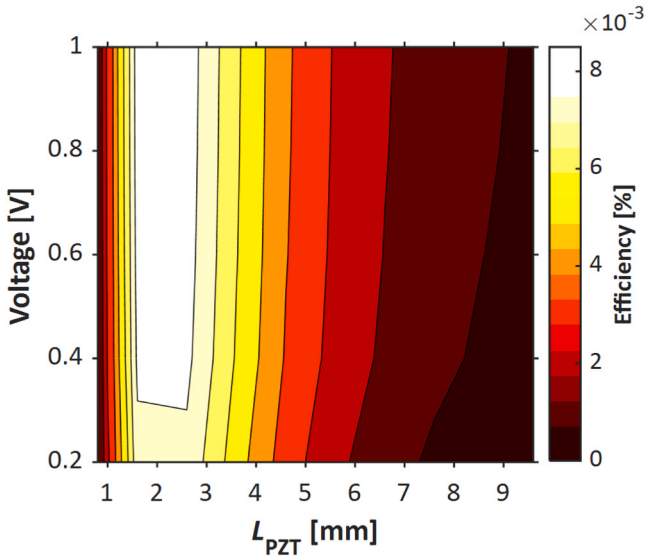

Fig. 8. Mechanical efficiency calculated from the mechanical and electrical energies as a function of the piezo stack length and input voltage.

force by the piezo stack. For $L_{PZT} > 6.6$ mm, the wide membrane caves in as a result of gravity, while the upward piezoelectric force is not enough to outperform the gravitational force. This is also shown in a 3D rendering of the displacement of the simulated ¼ devices in Fig. 5, where the largest device ($L_{PZT} = 9.6$ mm) in Fig. 5(d), displays less deflection at the center than off-center regions.

The electrical and mechanical energy components as well as the resulting mechanical efficiency as a function of the piezo stack length under various voltages are shown in Figs. 6, 7 and 8. The trend in Fig. 6 with regards to L_{PZT} shows that there is an optimal PZT area for each input voltage, which results in maximal output mechanical energy. For input voltages as high as 1 V, mechanical energy tends to be slightly less sensitive to L_{PZT} in the range of 4–9 mm. As explained above, the direct proportionality of Z_f and F_b with the input voltage leads to the mechanical energy being proportional to V^2.

The dependency of electrical energy on both voltage and L_{PZT} can be analyzed according to the principles governing parallel plate capacitors. First, ignoring the gravitational force and the deflection of the piezo stack under voltage excitation, the stack can be simplified with a parallel plate capacitor. In this case, the accumulated charge at the terminals will be

$$Q = CV = \frac{\varepsilon A}{d} V, \tag{4}$$

where ε is the electric permittivity of PZT, A is the area and d is the PZT thickness. Q therefore, is directly proportional to V and L_{PZT}^2, which means that according to Eq. (2), the electrical energy is proportional to L_{PZT}^2 and V^2. Taking the effect of gravity and the device deformations into account, one would expect slight changes to these deductions, especially for the case of larger devices and smaller input voltage, when the piezo stack is slightly different from a parallel plate capacitor due to deformations.

It is only reasonable to conclude that based on Eq. (3), the mechanical efficiency should be independent of the input voltage with the exceptions mentioned above and the optimal value should mostly depend on L_{PZT}. These deductions are confirmed in Fig. 8, where the largest efficiency values (0.008%) are achieved for $L_{PZT} \approx 2$ mm.

3.3. Diaphragm optimization

Another equally important parameter set for the device performance corresponds to the under-etched part of the substrate (the diaphragm).

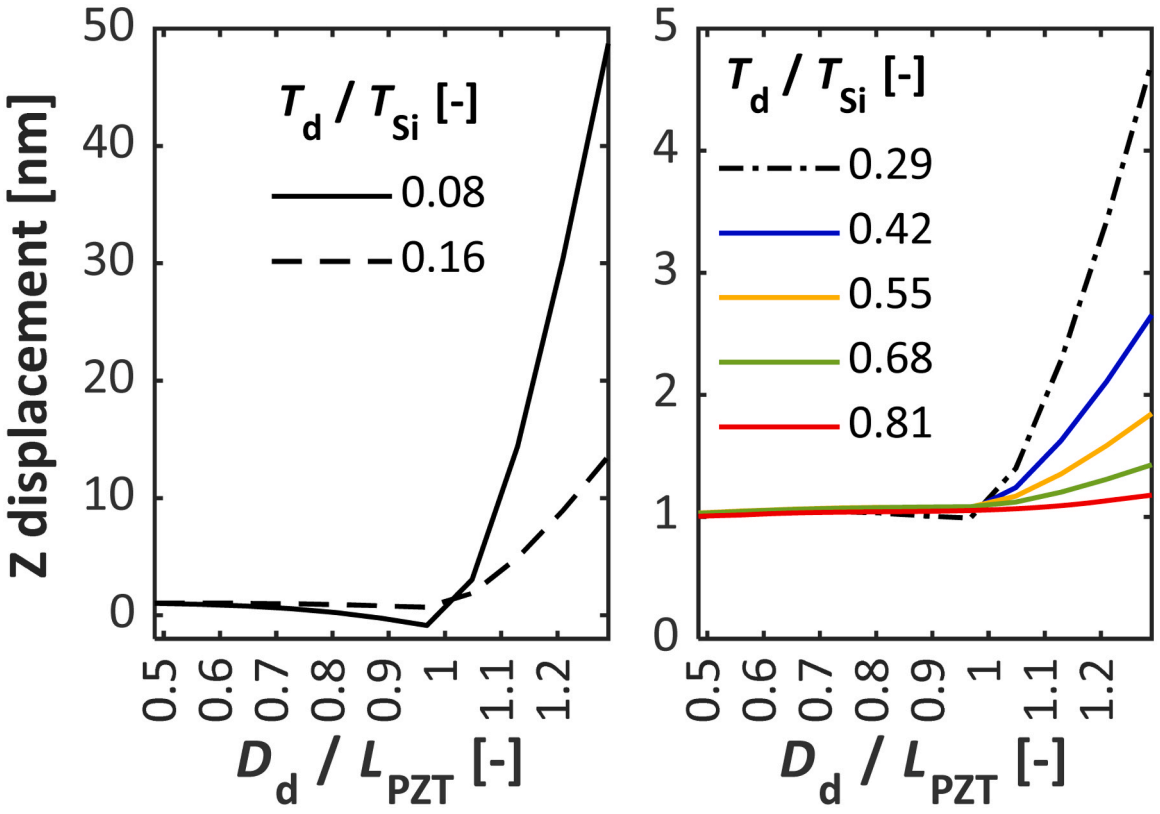

Fig. 9. Midpoint displacement as a function of diaphragm dimensions.

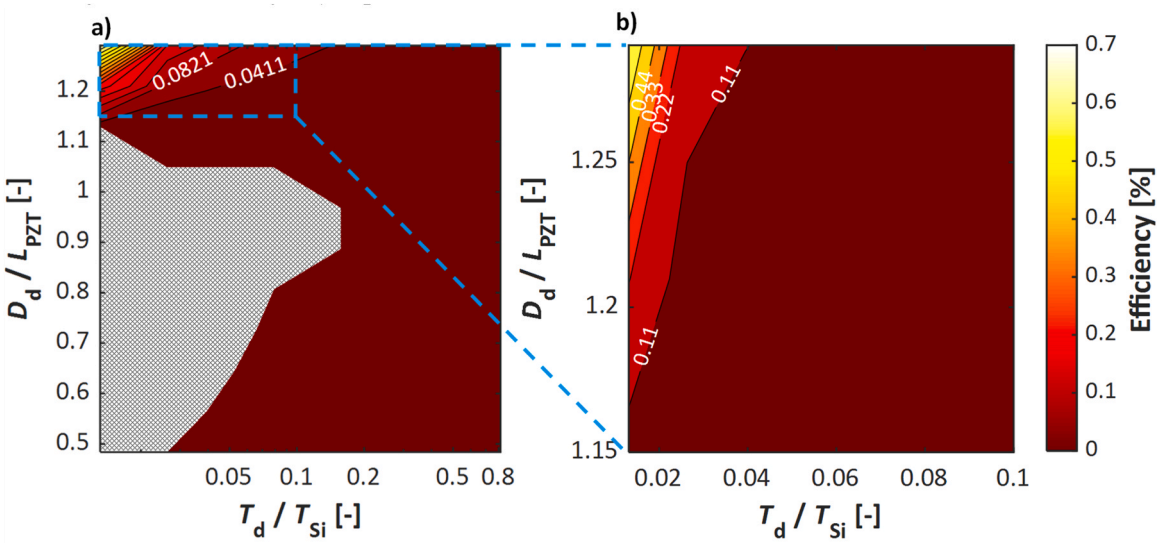

Fig. 10. a) mechanical efficiency as a function of diaphragm dimensions. The grey diamond pattern area marks invalid data points. b) enlarged area in the dashed rectangle from part a). The maximum mechanical efficiency at the top left corner is 0.65%.

In this section, we analyze the effect of variations in the diaphragm's thickness and diameter with respect to the substrate thickness (T_d/T_{Si}) and the piezo stack length (D_d/L_{PZT}), respectively. As mentioned before, the conditions for high output power and maximum efficiency are different and therefore, we keep L_{PZT} at the reference value (6.2 mm) and not 2 mm, obtained from the previous section, to maintain a reasonably high output power and sweep D_d from 3 to 8 mm. Additionally, T_d is varied from 30 to 310 μm. The resulting midpoint displacement is plotted in Fig. 9, with the data related to the thinnest two diaphragms on the left and the rest on the right-hand side for better visualization. Two conclusions are prominent here: i) for substantial increase in displacement, the diaphragm must be wider than the piezo stack, and ii) as seen in Fig. 9(left), for the thinnest diaphragms and when D_d is comparable to L_{PZT}, negative displacement is observed. This can be explained as such: the gravitational force is more effective on the thinner diaphragms, causing larger downward deflection in contrast to the piezoelectric effect. When the diameter is smaller, the sample's rigidity counteracts this downward deflection, keeping the total displacement at positive values. On the other hand, as we approach $D_d/L_{PZT} \approx 1$, rigidity is no longer effective and negative displacement

occurs. For wider diaphragms however, the clamping effect of the Si substrate is reduced, such that the piezo stack has more freedom to deflect upwards, resulting in significant increase in displacement. These observations are valid for even thinner diaphragms (down to 5 μm, corresponding to $T_d/T_{Si} = 0.013$), the results of which are not included in Fig. 9.

Since negative midpoint displacement is outside our desired range for deflections, we have not defined efficiency values for these datapoints. The efficiency graph for the acceptable datapoints is shown in Fig. 10. In this figure, all simulated diaphragm thicknesses from 5 to 310 μm are included. It should be noted that since the photodiode's p-n junction is part of the diaphragm, aggressive etching to reach very low thicknesses, is likely to damage the PV functionality of the device. For purely theoretical interest however, these datapoints are valuable. The grey diamond pattern area in Fig. 10(a) corresponds to invalid datapoints, where negative displacement is observed. The x-axis in this figure is in logarithmic scale for better visibility of the results for small T_d/T_{Si} values. A close up of the area marked with a dashed rectangle is presented in Fig. 10(b). As expected, for each T_d, the smallest efficiencies are achieved when $D_d/L_{PZT} \approx 1$. Moreover, thinner and wider diaphragms are required for highest efficiencies, as shown in Fig. 10(b). In the extreme case of $T_d/T_{Si} = 0.013$ and $D_d/L_{PZT} = 1.3$ (or $T_d = 5$ μm and $D_d = 8$ mm, the top left corner in Fig. 10(b)), the mechanical efficiency can reach 0.65%. This corresponds to a free displacement of 1.9 μm (a significant increase compared to the measured and simulated reference case of ~1 nm) and a blocking force of 18.5 μN. For a rather more practical case, when $T_d = 30$ μm ($T_d/T_{Si} = 0.08$), the mechanical efficiency can reach 0.06%, an almost 35 fold increase compared to the calculated mechanical efficiency for the reference device, i.e. 0.0017%.

4. Conclusion

In this work, we have presented a simulation approach for calculating the mechanical efficiency of on-chip piezo-photomotion devices in static conditions. The model parameters are calibrated with the experimentally measured displacement of our reference device, which consists of a 6.2 × 6.2 mm^2 thin-film PZT layer integrated with a silicon photodiode. This device displays an efficiency of 0.0017% with the free displacement and the blocking force equal to 1 nm and 92.64 μN, respectively.

An investigation into the effect of the PZT layer dimensions, while keeping the thickness of the backside etched area of the silicon substrate (the diaphragm) constant, reveals that the efficiency is highest when this layer is 2 × 2 mm^2. This is a result of the interplay between the gravitational force, the piezoelectric force and the input electrical energy, all of which vary with the piezo stack length. Additionally, the efficiency is almost independent of the input voltage. It should be noted that this optimum would change for a different diaphragm dimension or geometry.

The dimensions of the diaphragm have a more significant impact on efficiency, with a thickness of 30 μm and diameter of 8 mm (keeping the PZT area constant at 6.2 ×6.2 mm^2) leading to 0.06% mechanical efficiency, 48.8 nm free displacement and 68.4 μN blocking force. In a more aggressive etching scenario, when the diaphragm is as thin as 5 μm, the free displacement would see a sharp increase to 1.9 μm with a blocking force of 18.5 μN and a mechanical efficiency of 0.65%. These results can serve as a guideline in the design of future on-chip piezo-photomotion devices and eventually in light-driven micro and nanorobots. Depending on the application at hand, any of the abovementioned geometrical combinations can be employed. For example, in scenarios, where a high blocking force is needed, less aggressive substrate etching is recommended. On the other hand, for larger free displacement, wider and thinner diaphragms are preferred. In both cases, higher input voltage, e.g. using tandem solar cells is beneficial. It is worth noting that the mechanical efficiency as defined in this work is not the ultimate limit of such devices and therefore, a more efficient approach of extracting the produced mechanical work would result in considerably larger efficiency values.

CRediT authorship contribution statement

Nasim Rezaei: Conceptualization, Methodology, Software, Validation, Formal analysis, Data curation, Writing - original draft, Writing - review & editing, Visualization, **Zeinab Eftekhari:** Validation, Investigation **Jian-Yao Zheng:** Investigation, Resources **Rebecca Saive:** Conceptualization, Methodology, Writing - original draft, Writing - review & editing, Supervision, Project administration, Funding acquisition.

Declaration of Competing Interest

The authors declare that they have no known competing financial interests or personal relationships that could have appeared to influence the work reported in this paper.

Data availability

Data will be made available on request.

Acknowledgement

This publication is part of the project Piezo-photomotion (with project number VI.Vidi.193.020) of the research programme Vidi which is financed by the Dutch Research Council (NWO).

References

[1] H.H. Hariri, L.A. Prasetya, S. Foong, G.S. Soh, K.N. Otto, K.L. Wood, A tether-less legged piezoelectric miniature robot using bounding gait locomotion for bidirectional motion, 2016 IEEE Int. Conf. Robot. Autom. (ICRA) (2016) 4743–4749.
[2] D. Copaci, D. Blanco, L.E. Moreno, Flexible shape-memory alloy-based actuator: mechanical design optimization according to application, Actuators vol. 8 (3) (2019) 63.
[3] Z. Guo, Y. Pan, L.B. Wee, H. Yu, Design and control of a novel compliant differential shape memory alloy actuator, Sens Actuators A Phys. vol. 225 (2015) 71–80.
[4] M. Yazdani, A.F. Payam, A comparative study on material selection of microelectromechanical systems electrostatic actuators using Ashby, VIKOR and TOPSIS, Mater. Des. (1980-2015) vol. 65 (2015) 328–334.
[5] S.P. Burugupally, W.R. Perera, Dynamics of a parallel-plate electrostatic actuator in viscous dielectric media, Sens Actuators A Phys. vol. 295 (2019) 366–373.
[6] C. Pawashe, S. Floyd, M. Sitti, Modeling and experimental characterization of an untethered magnetic micro-robot, Int. J. Robot. Res. vol. 28 (8) (2009) 1077–1094, https://doi.org/10.1177/0278364909341413.
[7] G. Mao, et al., Soft electromagnetic actuators, Sci. Adv. vol. 6 (26) (2020), eabc0251.
[8] M. Sitti, D.S. Wiersma, Pros and Cons: Magnetic versus Optical Microrobots, in: Advanced Materials, vol. 32, Wiley-VCH Verlag, 2020, https://doi.org/10.1002/adma.201906766.
[9] D. Melling, J.G. Martinez, E.W.H. Jager, Conjugated Polymer Actuators and Devices: Progress and Opportunities. Advanced Materials, Wiley-VCH Verlag, 2019, https://doi.org/10.1002/adma.201808210.
[10] A. Bergander, W. Driesen, T. Varidel, and J.-M. Breguet, Monolithic piezoelectric actuators for miniature robotic systems, 2004.
[11] W. Jiang, F.M. Mayor, R.N. Patel, T.P. McKenna, C.J. Sarabalis, A.H. Safavi-Naeini, Nanobenders as efficient piezoelectric actuators for widely tunable nanophotonics at CMOS-level voltages, Commun. Phys. vol. 3 (1) (2020), https://doi.org/10.1038/s42005-020-00412-3.
[12] M.D. Nguyen, H.N. Vu, G. Rijnders, Nonlinearity in inverse and transverse piezoelectric properties of Pb(Zr0.52Ti0.48)O3 film actuators under AC and DC applied voltages, Curr. Appl. Phys. vol. 32 (2021) 106–110, https://doi.org/10.1016/j.cap.2021.10.007.
[13] W.M. Luiten, V.M. van der Werf, N. Raza, R. Saive, Investigation of the dynamic properties of on-chip coupled piezo/photodiodes by time-resolved atomic force and Kelvin probe microscopy, AIP Adv. vol. 10 (10) (2020), https://doi.org/10.1063/5.0028481.
[14] J. Qu, J. Choi, K.R. Oldham, Dynamic structural and contact modeling for a silicon hexapod microrobot, J. Mech. Robot vol. 9 (6) (2017), https://doi.org/10.1115/1.4037802.
[15] Z. Eftekhari, et al., Multimodal Kelvin probe force microscopy for spatial mapping of light-induced displacement in on-chip coupled piezo/photodiodes (vol. In submission), Beilstein J. Nanotechnol. (2023) (vol. In submission).

[16] F. Xu, F. Chu, S. Trolier-McKinstry, Longitudinal piezoelectric coefficient measurement for bulk ceramics and thin films using pneumatic pressure rig, J. Appl. Phys. vol. 86 (1) (1999) 588–594, https://doi.org/10.1063/1.370771.
[17] L. Lian, N.R. Sottos, Effects of thickness on the piezoelectric and dielectric properties of lead zirconate titanate thin films, J. Appl. Phys. vol. 87 (8) (2000) 3941–3949, https://doi.org/10.1063/1.372439.
[18] A.H.M. Smets, K. Jäger, O. Isabella, R.A. Swaaij, M. Zeman, Solar Energy: The Physics And Engineering of Photovoltaic Conversion, Technologies and Systems, UIT Cambridge, 2015.
[19] J.M. Russo, S.D. Vorndran, D. Zhang, M. Gordon, Y. Wu, R.K. Kostuk, Grating-over-lens holographic spectrum splitting concentrating photovoltaics, Renew. Energy Environ. (2013) RW1D.2, https://doi.org/10.1364/OSE.2013.RW1D.2.
[20] Z.J. Yu, K.C. Fisher, B.M. Wheelwright, R.P. Angel, Z.C. Holman, PVMirror: a new concept for tandem solar cells and hybrid solar converters, IEEE J. Photo vol. 5 (6) (2015) 1791–1799, https://doi.org/10.1109/JPHOTOV.2015.2458571.
[21] H. Helmers, et al., Pushing the boundaries of photovoltaic light to electricity conversion: a GaAs based photonic power converter with 68.9% efficiency, Conf. Rec. IEEE Photovolt. Spec. Conf. (2021) 2286–2289, https://doi.org/10.1109/PVSC43889.2021.9518920.
[22] Z. Yu, M. Leilaeioun, Z. Holman, Selecting tAndem Partners For Silicon Solar Cells, in: Nature Energy, vol. 1, Nature Publishing Group, 2016, https://doi.org/10.1038/nenergy.2016.137.
[23] H. Helmers, et al., 68.9% efficient gaas-based photonic power conversion enabled by photon recycling and optical resonance, Phys. Status Solidi - Rapid Res. Lett. vol. 15 (7) (2021), https://doi.org/10.1002/pssr.202100113.
[24] Z. Yang, S. Zhou, J. Zu, D. Inman, High-Performance Piezoelectric Energy Harvesters and Their Applications, in: Joule, vol. 2, Cell Press, 2018, pp. 642–697, https://doi.org/10.1016/j.joule.2018.03.011.
[25] Z. Yang, A. Erturk, J. Zu, On the efficiency of piezoelectric energy harvesters, Extrem. Mech. Lett. vol. 15 (2017) 26–37, https://doi.org/10.1016/j.eml.2017.05.002.
[26] M.W. Shafer, E. Garcia, The power and efficiency limits of piezoelectric energy harvesting, J. Vib. Acoust. vol. 136 (2) (2014), https://doi.org/10.1115/1.4025996.
[27] M. Kim, J. Dugundji, B.L. Wardle, Efficiency of piezoelectric mechanical vibration energy harvesting, Smart Mater. Struct. vol. 24 (5) (2015), https://doi.org/10.1088/0964-1726/24/5/055006.
[28] J. Xie, J. Yang, H. Hu, Y. Hu, X. Chen, A piezoelectric energy harvester based on flow-induced flexural vibration of a circular cylinder, J. Intell. Mater. Syst. Struct. vol. 23 (2) (2012) 135–139, https://doi.org/10.1177/1045389×11431744.
[29] S.J. Rupitsch, Topics in Mining, Metallurgy and Materials Engineering Piezoelectric Sensors and Actuators Fundamentals and Applications. [Online]. Available: ⟨http://www.springer.com/series/11054⟩.
[30] ⟨https://piezo.com/⟩.
[31] R.J. Wood, E. Steltz, R.S. Fearing, Optimal energy density piezoelectric bending actuators, Sens. Actuators A Phys. vol. 119 (2) (2005) 476–488, https://doi.org/10.1016/j.sna.2004.10.024.
[32] O. Seresta, S. Ragon, M.M. Abdalla, Z. Gürdal, D.K. Lindner, Design of a recurve actuator for maximum energy efficiency, Smart Mater. Struct. vol. 15 (6) (2006) 1919–1926, https://doi.org/10.1088/0964-1726/15/6/048.
[33] F.F.C. Duval, S.A. Wilson, G. Ensell, N.M.P. Evanno, M.G. Cain, R.W. Whatmore, Characterisation of PZT thin film micro-actuators using a silicon micro-force sensor, Sens. Actuators A Phys. vol. 133 (1,) (2007) 35–44, https://doi.org/10.1016/j.sna.2006.03.035.
[34] J. Xu et al., Triple-halide wide-band gap perovskites with suppressed phase segregation for efficient tandems, 2020. [Online]. Available: ⟨https://www.science.org⟩.
[35] B.M. Kayes et al., 27.6% Conversion efficiency, a new record for single-junction solar cells under 1 sun illumination, in *Conference Record of the IEEE Photovoltaic Specialists Conference*, 2011, pp. 000004–000008. ⟨doi:10.1109/PVSC.2011.6185831⟩.
[36] M. Wanlass, Systems and methods for advanced ultra-high-performance InP solar cells, 2017 [Online]. Available: ⟨https://www.osti.gov/biblio/1346013⟩.

Nasim Rezaei is a material modelling scientist at LayTec AG, Germany where she started working in 2023. Before that, she worked as a postdoc at the University of Twente on numerical simulations of light-driven piezoelectric actuators. She acquired her Master of Science degree in electrical engineering from Shiraz University, Iran, followed by a PhD degree in opto-electrical modelling of CIGS solar cells from Delft University of Technology.

Zeinab Eftekhari is a PhD candidate at the University of Twente, the Netherlands, where she has been working since 2021. Her focus lies on the application of scanning probe microscopy for the characterization of mechanical and optoelectronic responses of materials and devices. She obtained her Bachelor of Science degree in Physics from Urmia University, Iran, followed by a Master of Science degree in Applied Physics from Bilkent University, Turkey.

Jian-Yao Zheng is a material scientist who is currently a postdoctoral researcher at the University of Twente since 2021. He obtained his PhD degree from the Institute of Chemistry, Chinese Academy of Sciences (ICCAS) in 2012 and has prior postdoctoral experience at Trinity College Dublin (TCD) in Ireland (2012–2018) and AMOLF in the Netherlands (2018–2021).

Rebecca Saive is a professor of applied physics at the University of Twente, the Netherlands where she has been working since 2018. She graduated with her PhD from the University of Heidelberg in 2014 and subsequently became a postdoc and later senior scientist at the California Institute of Technology, USA.